Rational description of the ion-beam shaping mechanism

G. Rizza* and P. E. Coulon
Ecole Polytechnique, Laboratoire des Solides Irradiés, CEA-IRAMIS-CNRS, 91128 Palaiseau Cedex, France

V. Khomenkov, C. Dufour, I. Monnet, and M. Toulemonde
CIMAP-ENSICAEN-CEA-CNRS, University of Caen, Bd H. Becquerel, Boîte Postale 5133, 14070, Caen Cedex 5, France

S. Perruchas and T. Gacoin
Ecole Polytechnique, Laboratoire de Physique de la Matière Condensée, CNRS, 91128 Palaiseau Cedex, France

D. Mailly, X. Lafosse, and C. Ulysse
Laboratoire de Photonique et Nanostructures, CNRS, Marcoussis, France

E. A. Dawi
Debye Institute for Nanomaterials, Nanophotonics Section, Utrecht University, P.O. Box 80000, 3508 TA Utrecht, The Netherlands
(Received 10 November 2011; published 30 July 2012)

The ion-beam-shaping mechanism is studied for several classes of nearly monodispersed metallic nanoparticles (Au, Ag, and $Au_{0.5}Ag_{0.5}$). They are in the range of 3–100 nm and embedded within a silica matrix. Experimentally, we show that depending on their initial sizes, several final morphologies can be obtained: (i) spherical shapes, (ii) facetted nanoparticles, (iii) nanorods, and (iv) nanowires. In parallel, the thermal-spike model was implemented for three-dimensional anisotropic and composite media to study the evolution of the temperature profile within a nanoparticle. This way, a clear correlation is found between the deformation path followed by the nanoparticles during the irradiation and the fraction of the nanoparticle that is molten (vaporized) due to the interaction with a swift heavy ion. This allows the construction of a size-vs-shape diagram relating the initial nanoparticle size to its final morphology. This diagram is used to give a rational description of the ion-beam-shaping process for all nanoparticle dimensions as a function of the irradiation parameters.

DOI: 10.1103/PhysRevB.86.035450 PACS number(s): 61.82.Rx, 61.80.Jh, 68.37.Lp, 65.80.−g

I. INTRODUCTION

The development of the next generation of nanocomposites requires the fabrication of real three-dimensional embedded nanoarchitectures with spatially oriented geometries and well-defined topologically tunable properties. Nowadays, the limitations that are inherent to the standard nanostructuration techniques, like electron-beam lithography (EBL) or colloidal chemistry (CS), render this objective difficult to attain. In particular, EBL is *limited* to the fabrication of planar nanostructures whereas CS allows the synthesis of a large panel of nanoparticle (NP) shapes dispersed within liquid solutions. To overcome these limitations, several alternative strategies have been developed. Among them, ion-beam shaping represents an innovative approach to tune the morphology of embedded nanostructures. With this technique, spherical metallic NPs can be deformed into prolate nanorods and nanowires with an aspect ratio that can be tuned by varying the irradiation conditions. As the deformation takes place along the ion beam, the NPs can also be oriented within the matrix by simply changing the irradiation angle. The ion-beam-shaping phenomenon was first reported in 2001 by D'Orleans *et al.*[1] for Co NPs confined within a silica matrix irradiated with 200-MeV I ions. A detailed investigation of the irradiation-induced deformation has been carried out by Polman's group for NPs with a core-shell configuration, namely, a Au-core/silica-shell ($Au@SiO_2$) system (see, e.g., Refs. 2–4). The role of the NP size and density has been investigated by Dawi *et al.*[5] and by Rizza *et al.*[6] A theoretical interpretation of these experiments, based on the thermal-spike model, has been proposed by Awazu *et al.*[7] The thermodynamic properties of ion-shaped NPs have been studied by Ridgway's group with synchrotron techniques.[8–10] Rizza *et al.*have shown that depending on the initial size, several ion-shaped morphologies can be obtained.[11] Dawi *et al.*have investigated the relationship between the NP size and the energy deposited.[12] Ridgway *et al.*have demonstrated that the elongated NP width never exceeds the molten ion track diameter.[13] Finally, Dufour *et al.*have implemented the thermal-spike model in three dimensions and for anisotropic and composite media.[14]

In spite of the large number of publications existing in the literature, ion-beam shaping will only really become an alternative to the standard nanostructuration techniques if its capability to tune the features of the embedded NPs can clearly be demonstrated. Thus, the objective of this work is to give a rational description for the ion-beam-shaping mechanism. This is done by coupling experiments and simulations to show how the final NP shape is correlated to both its initial size and the irradiation conditions.

II. EXPERIMENTAL METHODS

Our sample is composed of chemically synthesized metallic NPs confined between two silica layers. Three classes of monodisperse metallic NPs (Au, Ag, and $Au_{0.5}Ag_{0.5}$) are investigated in this study. The standard synthesis technique for obtaining Au and Ag is the reduction of a metallic salt

TABLE I. Thermodynamic parameters. g is the electron-phonon coupling, K_e is the electronic thermal conductivity, N_{at} is the atomic density, E_m is the melting energy, and S_e is the electronic stopping power.

Element	g (W cm^{-3} K^{-1})	K_e (W cm^{-1} K^{-1})	N_{at} (10^{22} cm^{-3})	E_m (eV at^{-1})	S_e (keV nm^{-1}) for Kr ions of various energies in MeV 10	25	50	74	100	150	250
Au	2.3×10^{10}[a]	2.8[c]	5.90	0.433	6.9	14.4	22.0	26.3	28.3	30.7	32.7
Ag	3.3×10^{10}[a]	3.8[c]	5.86	0.385	6.4	13.0	19.2	22.1	23.3	24.2	24.7
$Au_{0.5}Ag_{0.5}$	2.8×10^{10}	3.3	5.88	0.409	6.6	13.7	20.6	24.2	25.8	27.5	28.7
SiO_2	2.2×10^{13}[b]	$3 \times 10^{-5}\ T_e$	$T_e < 7 \times 10^4$ K	(see Ref. 14)	3.6	6.5	8.5	9.2	9.6	9.9	10.0
SiO_2		2.0	$T_e > 7 \times 10^4$ K								

[a]Reference 23.
[b]Reference 22.
[c]Reference 24.

($HAuCl_4$ and $AgNO_3$, respectively) using a Turkevich-like method.[15,16] For obtaining Au-core/silver-shell (Au@Ag) NPs are synthesized.[17] Alloying is then induced by a thermal treatment.[6] The NPs with an average diameter in the range of 12–100 nm (size dispersion of 10%) are first grafted onto a 300-nm silica layer deposited onto a silicon substrate. Embedding is achieved by depositing a second silica overlayer of 300 nm onto the grafted structure. This way, all the NPs are confined within a single plane 300 nm below the sample surface (see, e.g., Refs. 6 and 12).

The samples have been irradiated both in the nuclear and in the electronic-stopping regimes. Irradiations at low energies (4-MeV Au ions) were carried out at the ARAMIS accelerator in Orsay, France. Irradiations at higher energies (74-MeV Kr ions) were done at the IRRSUD line at GANIL (France). In the latter case, the flux was kept constant at about 2×10^9 cm^{-2} s^{-1} in order to avoid the heating of the sample.

Table I summarizes the electronic stopping power (S_e), in both metallic NPs and silica matrix, for 10-250 MeV Kr ion irradiation. After preparation in cross-sectional geometry, samples were observed using a JEOL2010F transmission electron microscope (TEM), processed with a slow-scan CCD camera, and analyzed with a digital-micrograph program.

III. RESULTS

Figure 1 illustrates the morphological evolution of the embedded NPs as a function of both initial size (x axis) and irradiation fluence (y axis). The beam direction is indicated by the arrow. To extend our study to the domain of NPs smaller than 10 nm, a halo of satellites is created by preirradiating *some of the samples* with 4-MeV Au ions at a fluence of 5×10^{15} cm^{-2} [see, e.g., Ref. 18 and Figs. 1(d)–1(f)]. In a second stage, the ion-beam shaping is induced by irradiating *all the samples* at room temperature and normal incidence with 74-MeV Kr ions up to 5×10^{14} cm^{-2}.

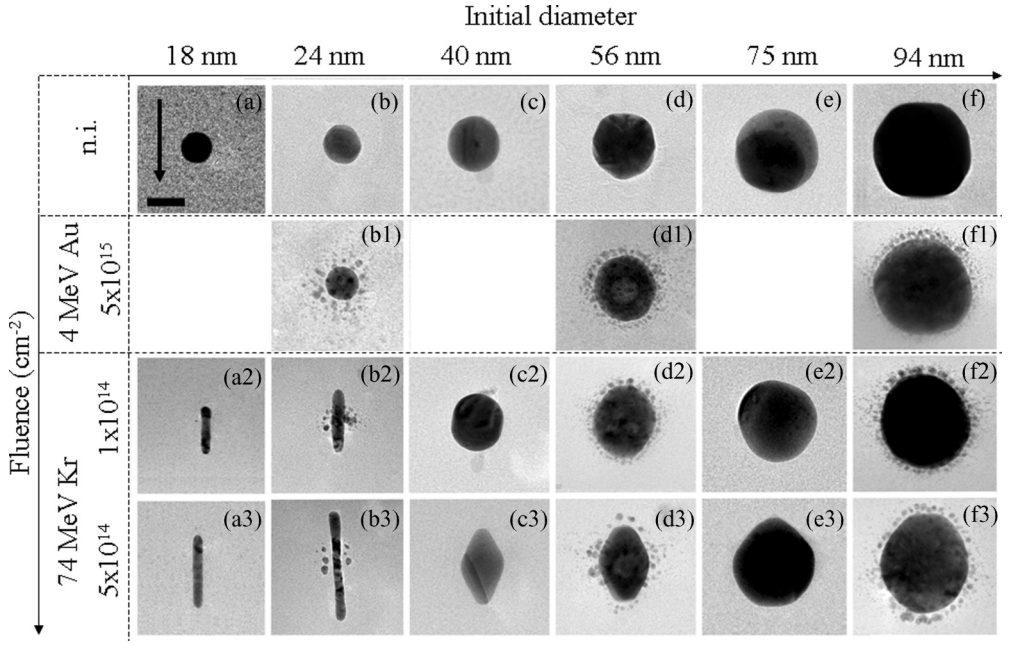

FIG. 1. Matrixlike diagram showing the morphological evolution of Au NPs for increasing initial size (x axis) and irradiation fluence (y axis). The length of the scale bar is 20 nm. The ion-beam direction is indicated by the arrow. Some of the samples [(b1), (d1), and (f1)] have been preirradiated with 4-MeV Au ions at 5×10^{15} cm^{-2} to create a halo of satellites around the central NPs (a2) to (f3). Afterward, all the samples have been irradiated up to 5×10^{15} cm^{-2} with 74-MeV Kr ions.

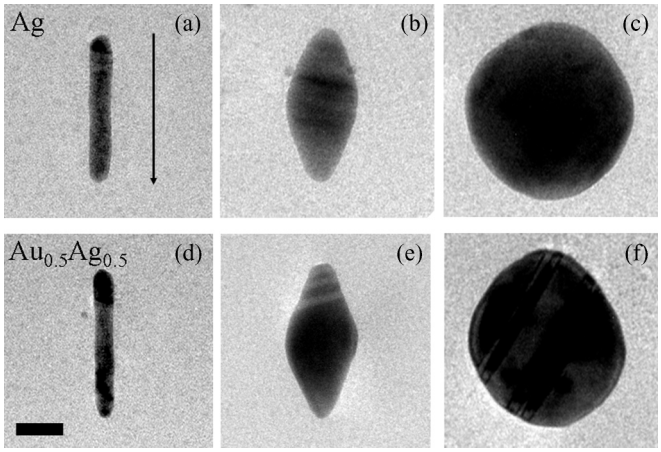

FIG. 2. Ion-beam-shaped Ag and $Au_{0.5}Ag_{0.5}$ NPs irradiated with 74-MeV Kr ions up to 5×10^{15} cm^{-2}. The initial sizes are (a) 20 nm, (b) 43 nm, and (c) 75 nm for the Ag NPs and (d) 18 nm, (e) 47 nm, and (f) 67 nm for the $Au_{0.5}Ag_{0.5}$ NPs. The length of the scale bar is 20 nm. The ion-beam direction is indicated by the arrow.

Clearly, a straightforward correlation exists between the initial size of a NP and its final morphology. In particular, four different deformation regimes can be observed.

(i) Satellites (<10 nm) remain spherical in shape no matter what the size of the "initial parent" NP.

(ii) NPs in the range 10–30 nm transform continuously into nanorods and nanowires.

(iii) When the NP size is further augmented (30–70 nm), an increasing refractoriness to deformation is observed. These NPs take longer times to be ion shaped and reveal a tendency to evolve toward facetted configurations.

(iv) Finally, larger NPs (>70–80 nm) are not noticeably deformed even at the highest irradiation fluence.

The same behavior is observed for Ag and $Au_{0.5}Ag_{0.5}$ NPs as shown in Fig. 2. Here, the ion-beam shaping is shown for three NP sizes in the range 18–80 nm irradiated with 74-MeV Kr ions up to 5×10^{14} cm^{-2}. Depending on their initial size, they evolve toward nanowires, i.e., regime (i); facetted NPs, i.e., regime (ii); or do not deform, i.e., regime (iii).

TEM micrographs indicate that the deformation rate is reduced when the initial NP size is increased. This behavior becomes more explicit if we plot the evolution of the normalized major axis $L(\Phi)/D_0$ as a function of the irradiation fluence Φ [Fig. 3(a)]. This is done for Au NPs. However, a similar behavior is also observed for Ag and $Au_{0.5}Ag_{0.5}$ NPs. To render the figure more readable, only a few NP sizes are reported. For all the configurations, the initial aspect ratio is equal to 1. However, its evolution with fluence is size dependent. For 29-nm Au NPs, it rises from 1 to 5.2 at a fluence of 5×10^{14} cm^{-2}. In other words, the dimension of the NP along the beam $L(\Phi)$ is 5.2 times larger than the initial diameter D_0. However, for initial sizes beyond about 30 nm, the deformation process becomes strongly reduced. For example, for 46-nm Au NPs the ratio $L(\Phi)/D_0$ barely exceeds 1.3 at 5×10^{14} cm^{-2}. Finally, 95-nm Au NPs do not deform, and $L(\Phi)/D_0$ remains close to 1.

Another way to visualize this behavior is to plot the maximum deformation length obtained at a fluence of 5×10^{14} cm^{-2}, L_{max}, as a function of the initial NP size D_0 [Fig. 3(b)]. We observe that up to about 30 nm, L_{max} rapidly increases with the NP size. However, above this value it progressively levels off toward its asymptotic value of 1.

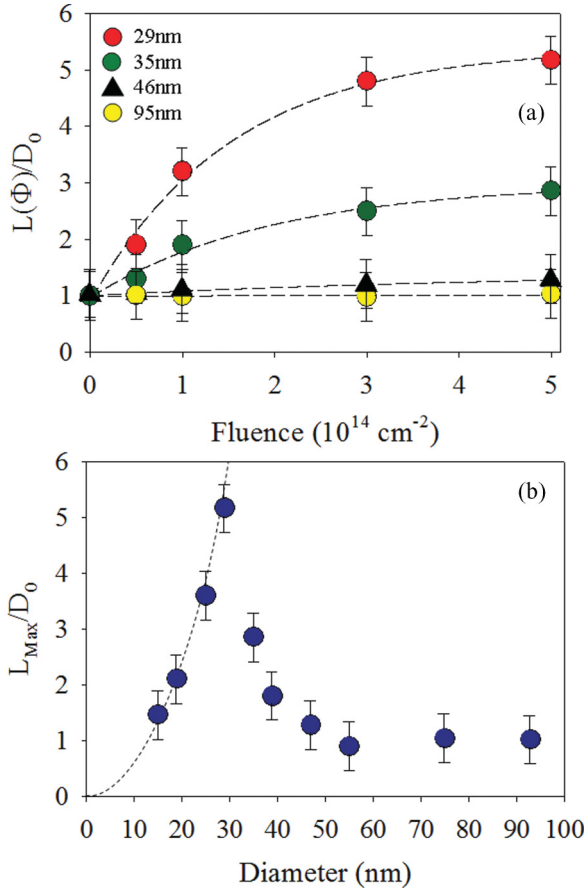

FIG. 3. (Color online) (a) Evolution of the normalized major axis $L(\Phi)/D_0$ as a function of the irradiation fluence Φ. (b) Evolution of the normalized maximum deformation length (L_{max}/D_0), obtained at a fluence of 5×10^{14} cm^{-2}, as a function of the initial NP size, D_0.

IV. DISCUSSION

The commonly accepted model for the ion-beam-shaping mechanism considers the flow of the metallic species within the liquid ion track in silica (see, e.g., Refs. 1,2,19,20). If this mechanism is correct, a spherical NP of volume $V_{sphere} = (4/3)\pi R_0^3$ is transformed into a nanowire of cylindrical shape of volume $V_{cyl} = \pi R_{cyl}^2 L_{max}$. Thus, the maximum length of the nanowire L_{max} must scale as

$$L_{max} = \frac{4}{3R_{cyl}^2} R_0^3. \quad (1)$$

$2R_{cyl}$ corresponds to the width of the elongated NP. Ridgway *et al.*[13] have shown that this value evolves toward a minimum sustainable metal-specific value, e.g., $2R_{cyl} = 10$ nm for Au NPs. Hence, the radius of the cylinder can be taken as a constant ($R_{cyl} = 5$ nm) while L_{max} must then scale with the cube of the initial NP size, i.e., R_0^3. This scaling law is reported as a dotted line in Fig. 3(b). Clearly, the experimental data fit Eq. (1) only up to about 30 nm. This is a strong indication

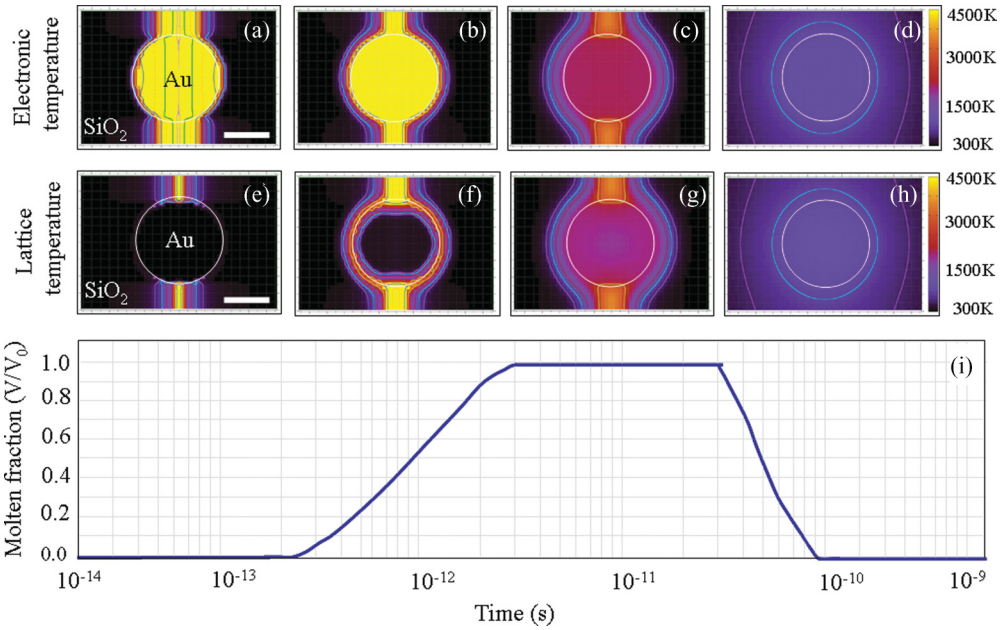

FIG. 4. (Color online) Timeline of the thermal evolution for a 20-nm Au NP embedded within a SiO_2 matrix irradiated with a 74-MeV Kr ion. Simulations have been run considering an ion intercepting the NP at the pole. (a)–(d) electronic temperature and (e)–(h) lattice temperature. (i) Time evolution of the fraction of the NP that reaches a temperature larger than that of melting, i.e., the molten fraction.

that the basic mechanism underlying the ion-beam-shaping process must be reconsidered. We will see in the next sections how these results can be interpreted within a more general description of the ion-beam-shaping phenomenon.

A. Timeline thermal evolution of an irradiated NP

It is obvious that for the fabrication of ion-beam-shaped nanocomposites with tailor-made properties, a rational description of their behavior is crucial. With this objective in mind, the thermal evolution of an embedded NP interacting with a swift heavy ion (SHI) is simulated using a three-dimensional implementation of the thermal-spike model (3D-TS) developed for anisotropic and composite media.[14] As an example, the thermal evolution for a 20-nm Au NP irradiated with 74-MeV Kr ions is shown in the form of a set of snapshots in a cross-section view in Figs. 4(a)–4(i). The same simulations have also been performed for Ag and $Au_{0.5}Ag_{0.5}$ NPs. All the thermodynamic parameters used for simulations are reported in Table I. Basically, most of the SHI energy deposited by the impinging ion is absorbed by the electrons of the target material. Thus, the first row shows the time evolution for the electronic temperature [Figs. 4(a)–4(d)]. Afterward, this energy is dissipated through two main competitive channels: electronic heat diffusion and electron-phonon interaction. Thus, the second row shows the time evolution for the lattice temperature [Figs. 4(e)–4(h)]. Finally, in Fig. 4(i), the fraction of the NP that reaches a temperature larger than that of melting is reported.

For times shorter than about 3×10^{-13} s, a cylindrical hot region is formed within the silica matrix around the ion trajectory, i.e., the latent track. In the meantime, the lattice temperature within the metallic NP does not change noticeably, and the NP remains in a solid state [Fig. 4(e)]. For times larger than about 2×10^{-13} s, the NP begins to melt starting from its surface [Fig. 4(f)]. In the next stage, the liquid layer diffuses toward the center of the NP, which becomes completely molten for times larger than 3×10^{-12} s. The liquid phase lasts up to 2×10^{-11} s [Fig. 4(g)]. Finally, the NP thermalizes, reaching the equilibrium temperature at 2×10^{-10} s [Fig. 4(h)].

B. Phenomenological description of the ion-embedded NP interaction

A phenomenological description of the physics behind the simulation results is obtained by using the schematic diagram of Fig. 5. We first analyze the results for the silica matrix and then those for the Au NPs.

The localization of the hot region in silica is schematized in Fig. 5(a). Silica possesses a low electronic thermal conductivity K_e and a high value for the electron-phonon coupling constant g.[14] Thus, the deposited energy remains spatially localized within the ion trajectory where it is rapidly

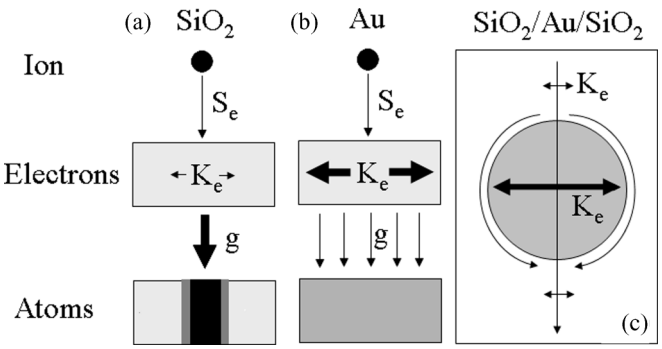

FIG. 5. Schematic diagram for the swift-heavy-ion–matter interaction for (a) bulk silica, (b) bulk gold, and (c) gold NPs confined within a SiO_2 matrix.

thermalized, resulting in a narrow and hot ion track. Here, the temperature exceeds the vaporization temperature, $T_{vap} = 3223$ K, within a distance of 2.5 nm and remains larger than the melting temperature, $T_{melt} = 1972$ K, up to 5 nm from the ion path. Thus, a value of about 10 nm for the diameter of the molten phase is obtained. Using this value as the definition for the ion track, our estimate is in excellent agreement with both previous simulations and experimental estimates.[21,22]

In contrast with silica, gold possesses a high value for the electronic thermal conductivity and a weak electron-phonon coupling.[14] Thus, the deposited energy is swiftly smeared out over the electronic subsystem while it is only weakly coupled to the atomic subsystem [Fig. 5(b)]. This results in a rapid increase of the electronic temperature but in a limited augmentation of the lattice temperature.

The scenario for the Au NPs embedded within a silica matrix leads to an interesting effect [Fig. 5(c)]. The energy transferred to the electrons of a Au NP diffuses rapidly outwards to the surface. When this energy reaches the Au/SiO_2 interface, it is transferred to the electrons of the neighboring silica matrix. Here, the large electron-phonon coupling results in the formation of a hot silica layer. Thus, the dielectric matrix acts as a barrier for the diffusion of the electronic energy, allowing, at the same time, its transformation into heat. Then, in a further stage the heat diffuses back toward the center of the NP.

Thus, we can conclude that the irradiation-induced heating of a gold NP (high K_e, low g) confined within a silica matrix (low K_e, high g) can be seen as an indirect mechanism wherein both the NP and the surrounding matrix participate in the process. Due to this *indirect-heating mechanism*, the temperature profile within the NP becomes strongly size dependent.

C. Construction of an initial-size versus final-morphology diagram for an ion impacting the NP at its center

At this point, 3D-TS simulations are used to determine the highest temperature reached within an embedded NP as a function of its size. This is shown in Fig. 6 for Au NPs ranging from 10 to 100 nm. (Similar simulations have also been done for Ag and $Au_{0.5}Ag_{0.5}$ NPs.) From these simulations

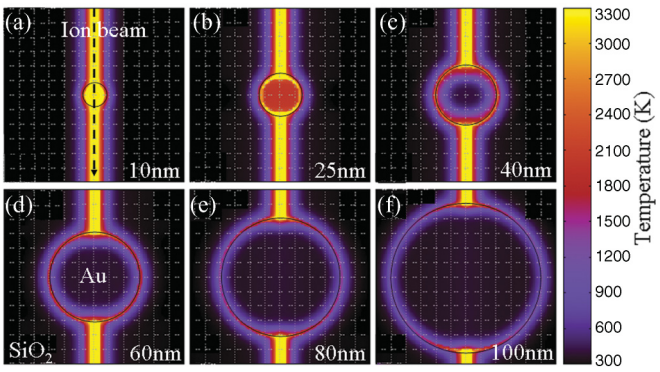

FIG. 6. (Color online) Each panel represents the 3D-TS simulation corresponding to the highest temperature reached within the Au NPs. The ion trajectory is indicated by the dotted arrow. The sizes of the NPs are (a) 10 nm, (b) 25 nm, (c) 40 nm, (d) 60 nm, (e) 80 nm, and (f) 100 nm.

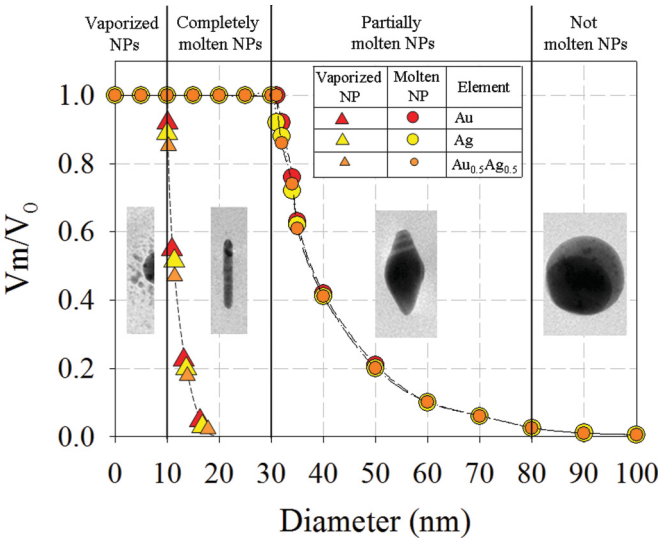

FIG. 7. (Color online) The size-vs-shape diagram used to rationalize the ion-beam-shaping process for all the NP sizes. Four temperature-dependent regions can be defined: (i) vaporized NPs (1–10 nm) conserve their spherical shape, (ii) completely molten NPs (10–30 nm) transform into nanorods and/or nanowires, (iii) partially molten NPs (30–80 nm) evolve toward facetted NPs, and (iv) not molten NPs (>80 nm) do not deform, or their deformation rate is very low. The vaporized fraction is represented by triangles whereas the molten fraction is represented by circles.

we obtain the fraction of the NPs that have been vaporized (full triangles) or molten (full circles) as a function of the initial NP size, D_0 (Fig. 7). Finally, comparing the experimental results from Fig. 1 with the vaporized/molten fractions from Fig. 7, a clear correspondence appears between the initial NP size and its deformation path. Thus, the ion-beam-shaping mechanism can be rationalized as follows.

(i) The energy deposited by the impinging ion is sufficient to vaporize Au NPs smaller than 10 nm [Fig. 6(a)]. These NPs do not deform and remain spherical in shape. This behavior is observed for the halo of satellites surrounding the central NP.

(ii) Beyond this diameter and for sizes up to 30 nm, the NPs are completely molten [Fig. 6(b)]. Completely molten NPs deform into nanorods and nanowires aligned along the ion beam. Within this size range, the ion-beam shaping is more likely due to the flow of the metallic species within the liquid ion track in silica. It is worth noting that this mechanism has already been proposed by other groups.[1,2,19,20] However, we show here that this mechanism is only valid for completely molten NPs.

(iii) For larger sizes, the efficiency of the process decreases with the dimension of the NP, and the molten region no longer reaches the core of the NP such that it remains solid [Fig. 6(c)]. Thus, NPs larger than 30 nm are only partially molten, and the thickness of the liquid layer decreases with the NP size [Figs. 6(d) and 6(e)]. For example, for a 35-nm Au NP, it is about 6 nm (75% of its volume). This values reduces to 2 nm for a 50-nm Au NP (23% of the volume) and to about 1 nm for a 60-nm Au NP (10% of the volume). If we accept that the flow mechanism is the driving force for the ion-beam-shaping process, then the deformation rate decreases with the fraction of the melt, i.e., with the increase of the solid core. On the

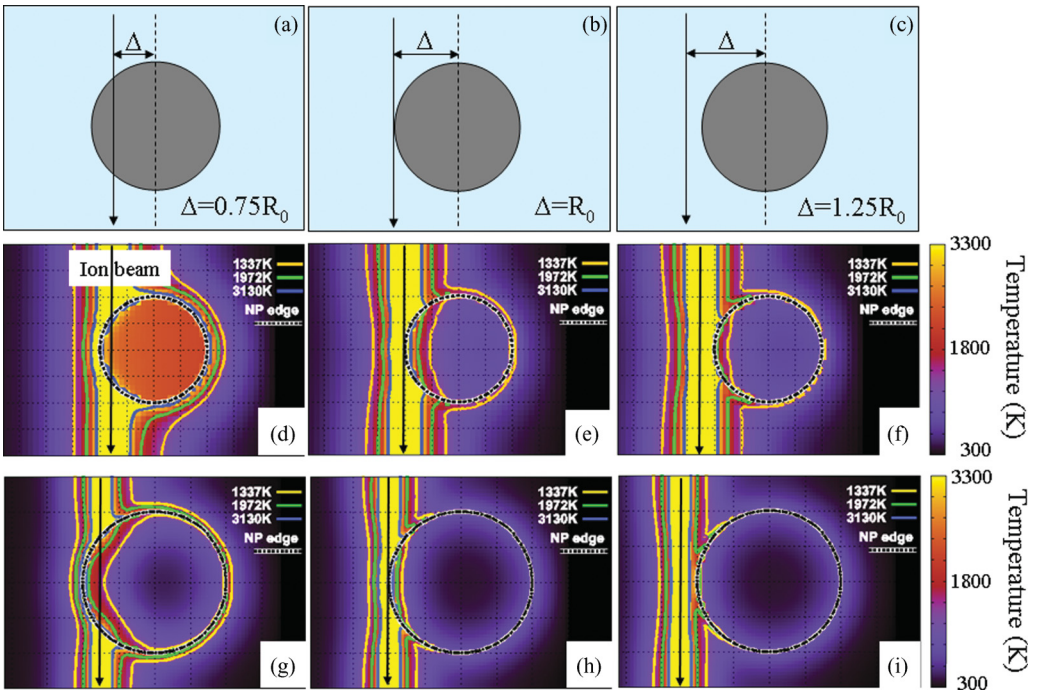

FIG. 8. (Color online) (a)–(c) SHI-NP interaction as a function of the ion-path distance from the NP center with $\Delta = 0.75R_0$, R_0, and $1.25R_0$. Here, R_0 is the NP radius. These values correspond to three specific impact conditions: (i) within the NP ($\Delta = 0.75R_0$), (ii) at the edge of the NP ($\Delta = R_0$), and (iii) in the proximity of the NP ($\Delta = 1.25R_0$). 3D-TS simulations corresponding to the maximum lattice temperature are shown for (d)–(f) 20-nm and (g)–(i) 40-nm Au NPs irradiated with a 74-MeV Kr ion.

other hand, the morphology of an irradiated NP evolves toward a facetted shape.[11]

(iv) Finally, for Au NPs larger than 80 nm, the thickness of the molten layer is negligible, i.e., less than 0.2 nm (<2% of the volume) [Fig. 6(f)]. Here, the molten layer is as thin as 0.2 nm or less such that the deformation process becomes strongly reduced or inefficient. In this case NPs either do not deform, or their deformation rate is extremely slow.

To conclude this section, it is worth mentioning that the previous simulations have been performed assuming a single ion impact. In reality, the whole deformation process necessitates the accumulation of hundreds of impacts for the ion-beam shaping to be effective. For example, irradiation fluences larger than 10^{14} cm^{-2} are necessary to transform a spherical NP into a nanorod or a nanowire.

D. Construction of an initial-size versus final-morphology diagram for an off-axis ion impact

So far we have analyzed the temperature evolution of an irradiated NP considering an ion passing through its center. In the following, we focus on the effect of an off-axis ion impact. Simulations were performed for three offset values ($\Delta = 0.75R_0$, R_0, and $1.25R_0$) [Figs. 8(a)–8(c)]. These values correspond to three specific impact conditions: (i) within the NP ($\Delta = 0.75R_0$), (ii) at the edge of the NP ($\Delta = R_0$), and (iii) in the proximity of the NP ($\Delta = 1.25R_0$). The corresponding 3D-TS simulations are shown for two NP sizes, 20 and 40 nm, in Figs. 8(d)–8(i). The first remark is that for noncentral impacts, the melting of the particle still starts from the NP surface. On the other hand, the lattice temperature significantly increases only if the ion path effectively intercepts the NP, i.e., $\Delta \leqslant R_0$.

A diagram describing the molten (vaporized) fraction as a function of the NP size can also be drawn for off-axis impacts. This is shown in Fig. 9 for offset values Δ, ranging from 0 to $1.5R_0$. First, it makes a difference if the ion does or does not intercept the NP, i.e., if $\Delta < R_0$ or $\Delta > R_0$. For Δ increasing from 0 to $0.75R_0$, a slight reduction of the maximum

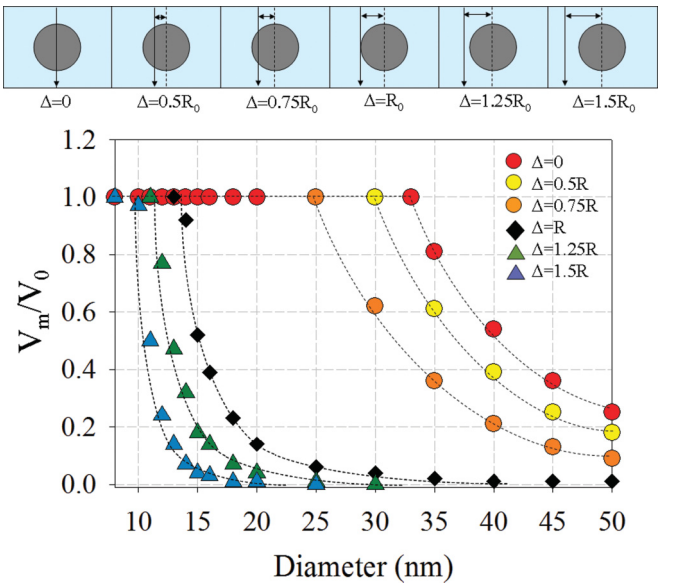

FIG. 9. (Color online) The size-vs-shape diagram for an off-axis impact Δ, varying from 0 to $1.5R_0$. Au NPs are irradiated with a 74-MeV Kr ion.

molten-NP size is observed. In particular, this value is reduced from 33 nm for $\Delta = 0$ to about 25 nm for an ion impact at $\Delta = 0.75R_0$. However, as soon as the ion hits the NP at its edge $\Delta = R_0$, an abrupt reduction for the largest molten-NP size is observed. Here, it barely exceeds a diameter of 14 nm. If Δ is further increased, ($\Delta = 1.25R_0$ and $1.5R_0$), i.e., the ion passes close to but without interacting with the NP, the largest molten NP is reduced to about 10 nm.

Thus, we can conclude that for an efficient melting process, the ion must depose its energy within the NP.

E. Size-vs-shape diagram: Chemical composition and irradiation conditions

Let us check now how the diagram of Fig. 7 is modified when the chemical composition of the NP and/or the irradiation energy are changed. This can be understood by considering the ratio between the deposited energy E_d and the melting energy E_m:[14]

$$k = \frac{E_d}{E_m} = \frac{6S_e}{\pi N_{\text{at}} D^2 E_m}, \tag{2}$$

where S_e is the electronic stopping power, N_{at} is the atomic concentration, and D is the NP size. If E_d is larger than E_m ($k \geqslant 1$), the NP will be completely molten. Otherwise, the melting will be only partial ($k < 1$). However, Eq. (2) is a crude approximation. It is valid when the deposited energy S_e remains confined within the NP. However, strong energy leakage occurs because of the energy transfer to the electrons of the surrounding SiO_2 matrix. Besides, in high-energy irradiations, the radial distribution of the δ electron may be larger than the dimension of the NP. Thus, in reality a complete melting occurs for a value of k that is larger than 1. Full 3D-TS simulations give an effective value for k of $\sim$1.9. Figure 7 shows that the evolution of the molten fraction is almost the same for the three classes of NPs (Au, Ag, and $Au_{0.5}Ag_{0.5}$). Here, $E_m(\text{Au})/E_m(\text{Ag}) = 1.17$, $E_d(\text{Au})/E_d(\text{Ag}) = 1.13$, and the E_d/E_m ratio is almost the same for all three materials. Thus, we can expect similar molten-volume fractions for Au and Ag NPs of the same size. However, for other kinetic energies, S_e is changed, and the diagrams will be different. For example, for an irradiation with 250-MeV Kr ions, the ratio $E_d(\text{Au})/E_d(\text{Ag})$ becomes 1.33, and the maximum molten diameter for Au NPs becomes larger than that for Ag NPs.

F. Tuning the size-vs-shape diagram

The size-vs-shape diagram of Fig. 7 represents the vaporized/molten fraction for a given ion energy. This result can be generalized for a larger range of ion energies. In Figs. 10(a) and 10(b), the diagram is plotted for Kr-ion energies varying from 10 to 250 MeV, i.e., from 0 to 3.5 MeV u^{-1}. We observe that when the ion energy is increased (reduced), the diagram is expanded (contracted). For example, for an irradiation with 10-MeV Kr ions, the maximum molten diameter is 14.7 nm for Au NPs (15.5 nm for Ag NPs). This value is increased to 31 nm for Au NPs (32 nm for Ag NPs) at 74-MeV Kr ions. If the ion energy is further increased, the maximum molten diameter becomes less dependent on the deposited energy, reaching a plateau (31.5 nm and 34.5 nm for Au and Ag NPs at 250-MeV Kr ions, respectively). This result has an important practical consequence: the diagram can be either expanded or contracted by simply changing the energy of the impinging ions.

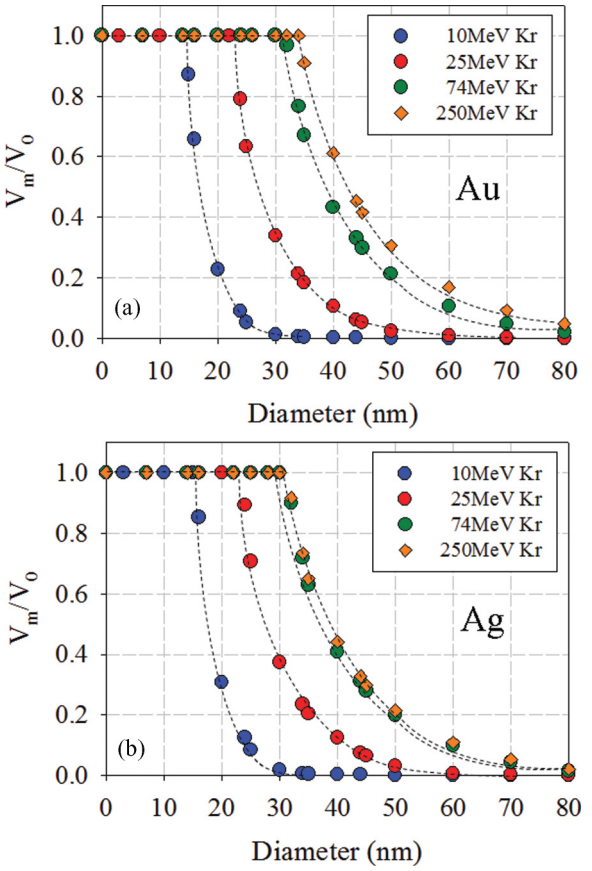

FIG. 10. (Color online) The size-vs-shape diagram for both (a) Au NPs and (b) Ag NPs by varying the ion energy (10–250-MeV Kr ions).

Thus, using the data of Fig. 10, a size-vs-shape diagram can be built as a function of the ion energy (Fig. 11). In particular, as the domain extension of the different regimes is both energy and size dependent, this diagram gives us the key to control

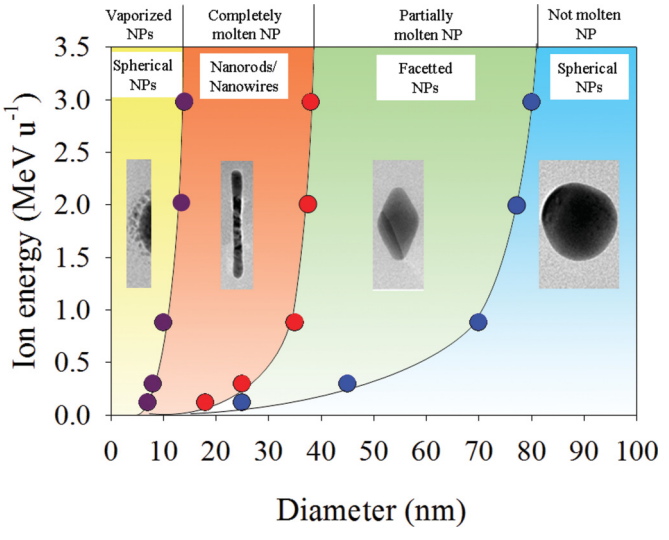

FIG. 11. (Color online) Evolution of the size-vs-shape diagram when both the NP size and the ion energy are varied.

the transition between the different deformation regimes (elongated, facetted, and spherical) and thus to precisely tune the final shape of the embedded NPs.

On the other hand, the other irradiation parameters, such as the ion flux and the temperature, do not directly change the diagram. However, they can be used to modify the kinetics of the ion-beam-shaping process.

V. CONCLUSIONS

In conclusion, in this work we have addressed the problem of how to rationalize the ion-beam-shaping mechanism. Our objective was achieved by coupling a model system composed of nearly monodispere metallic NPs embedded within a silica matrix to a real 3D implementation of the thermal-spike model devoted to the simulation of swift-heavy-ion interaction.

First, we built a matrixlike diagram to correlate the final ion-beam-shaped morphology to both the initial NP size and the irradiation fluence (Fig. 1). In a second step, 3D-TS simulations are used to obtain the dependence of the vaporized/molten fraction on the initial NP size (Fig. 7). Finally, the direct comparison between these two results allows the characterization of several deformation regimes for the ion-shaping mechanism.

(i) Very small NPs are completely vaporized and remain spherical in shape upon irradiation.

(ii) Completely molten NPs transform into nanorods and subsequently, for increasing fluence, into nanowires.

(iii) Partially molten NPs transform into facetted NPs.

(iv) Very large NPs do not melt and do not deform, or their deformation rate is very low.

The extension of each regime (i)–(iv) depends on both the NP composition and the irradiation parameters, such as the ion energy and the irradiation fluence (Fig. 11). In particular, we have shown that the ion-shaping mechanism is effective only if the ion deposes its energy within the NP. The other irradiation parameters, such as the ion flux or the temperature, only modify the deformation kinetics but not the size-vs-shape diagram. As the size-vs-shape diagram can be tuned through the proper choice of experimental conditions, the final NP morphology can also be monitored.

Finally, this work represents a step forward in the development of an alternative route, with respect to standard nanolithography and colloidal-chemistry techniques, to the controllable fabrication of a whole family of embedded nanostructures in vertical geometries with topologically tunable properties.

ACKNOWLEDGMENTS

We wish to thank G. Coddens (LSI-Ecole Polytechnique) for many fruitful discussions. This work was supported by the French National Research Agency under contract No. ANR-09-BLANC-0334 and by the METSA network for the microscopy facilities.

*giancarlo.rizza@polytechnique.edu

[1] C. D'Orléans, J. P. Stoquert, C. Estournès, C. Cerruti, J. J. Grob, J. L. Guille, F. Haas, D. Muller, and M. Richard-Plouet, Phys. Rev. B **67**, 220101(R) (2003).

[2] S. Roorda, T. van Dillen, A. Polman, C. Graf, A. M. Vredenberg, A. van Blaaderen, and B. Kooi, Adv. Mater. (Weinheim, Ger.) **16**, 235 (2004).

[3] J. J. Penninkhof, T. van Dillen, A. Polman, C. Graf, and A. van Blaaderen, Adv. Mater. (Weinheim, Ger.) **17**, 1484 (2005).

[4] J. J. Penninkhof, T. van Dillen, S. Roorda, C. Graf, A. van Blaaderen, A. M. Vredenberg, and A. Polman, Nucl. Instr. Methods Phys. Res., Sect. B **242**, 523 (2006).

[5] E. A. Dawi, G. Rizza, M. P. Mink, A. M. Vredenberg, and F. H. P. M. Habraken, J. Appl. Phys. **105**, 074305 (2009).

[6] G. Rizza, F. Attouchi, P.-E. Coulon, S. Perruchas, T. Gacoin, I. Monnet, and L. Largeau, Nanotechnology **22**, 175305 (2001).

[7] K. Awazu, X. Wang, M. Fujimaki, J. Tominaga, H. Aiba, Y. Ohki, and T. Komatsubara, Phys. Rev. B **78**, 054102 (2008).

[8] R. Giulian, P. Kluth, L. L. Araujo, D. J. Sprouster, A. P. Byrne, D. J. Cookson, and M. C. Ridgway, Phys. Rev. B **78**, 125413 (2008).

[9] M. C. Ridgway, P. Kluth, R. Giulian, D. Sprouster, L. L. Araujo, C. Schnohr, D. Llewellyn, A. Byrne, G. Foran, and D. Cookson, Nucl. Instrum. Methods Phys. Res., Sect. B **267**, 931 (2009).

[10] D. Sprouster, R. Giulian, L. L. Araujo, P. Kluth, B. Johannessen, D. Cookson, and M. C. Ridgway, J. Appl. Phys. **109**, 113504 (2011).

[11] G. Rizza, E. A. Dawi, A. M. Vredenberg, and I. Monnet, Appl. Phys. Lett. **95**, 043105 (2009).

[12] E. A. Dawi, A. M. Vredenberg, G. Rizza, and M. Toulemeonde, Nanotechnology **22**, 215607 (2011).

[13] M. C. Ridgway, R. Giulian, D. J. Sprouster, P. Kluth, L. L. Araujo, D. J. Llewellyn, A. P. Byrne, F. Kremer, P. F. P. Fichtner, G. Rizza, H. Amekura, and M. Toulemonde, Phys. Rev. Lett. **106**, 095505 (2011).

[14] C. Dufour, V. Khomenkov, G. Rizza, and M. Toulemonde, J. Phys. D **45**, 065302 (2012).

[15] J. Turkevich, P. Cooper Stevenson, and J. Hillier, Discuss. Faraday Soc. **11**, 55 (1951).

[16] C. Ziegler and A. Eychmüller, J. Phys. Chem. C **115**, 4502 (2011).

[17] F. Hubenthal, N. Borg, and F. Träger, Appl. Phys. B **93**, 39 (2008).

[18] G. Rizza, H. Cheverry, T. Gacoin, A. Lamasson, and S. Henry, J. Appl. Phys. **101**, 14321 (2007).

[19] S. Klaumünzer, Nucl. Instrum. Methods Phys. Res., Sect. B **244**, 1 (2006).

[20] R. Giulian, F. Kremer, L. L. Araujo, D. J. Sprouster, P. Kluth, P. F. P. Fichtner, A. P. Byrne, and M. C. Ridgway, Phys. Rev. B **82**, 113410 (2010).

[21] P. Kluth, R. Giulian, D. J. Sprouster, C. S. Schnohr, A. P. Byrne, D. J. Cookson, and M. C. Ridgway, Appl. Phys. Lett. **94**, 113107 (2009).

[22] M. Toulemonde, W. J. Weber, G. S. Li, V. Shutthanandan, P. Kluth, T. F. Yang, Y. G. Wang, and Y. W. Zhang, Phys. Rev. B **83**, 054106 (2011).

[23] Z. Wang, C. Dufour, E. Paumier, and M. Toulemonde, J. Phys.: Condens. Matter **6**, 6733 (1994).

[24] D. R. Lide, ed., *CRC Handbook of Chemistry and Physics*, 86th ed. (CRC, Boca Raton, FL, 2005).